Volume 1 | Number 1 | Jan 2013 | Pages 1–100

Journal of
Materials Chemistry A

Materials for energy and sustainability
www.rsc.org/materialsA

ROYAL SOCIETY
OF CHEMISTRY

ROYAL SOCIETY
OF CHEMISTRY

www.rsc.org/materialsA

Journal Name

ARTICLE

Composites of Boron-doped Carbon Nanosheets and Iron Oxide Nanoneedles: Fabrication and Lithium Ion Storage Performance

Yongqiang Yang,[a] Jianan Zhang, [a] Xiaochen Wu, [a] Yongsheng Fu,[b] Haixia Wu [a,*], and Shouwu Guo,[a,b,*]

Novel boron-doped carbon nanosheets were prepared through a facile hydrothermal method using glucose and sodium borohydride as precursors. Taking structural advantage of the as-prepared boron-doped carbon nanosheets, the high density Fe_3O_4 nanoneedle arrays were generated on them, resulting in the composites of boron-doped carbon nanosheets/Fe_3O_4 nanoneedles. The nanoneedle-like morphology and the unique perpendicular orientation of the Fe_3O_4 nanoneedles suppressed largely the aggregation of the boron-doped carbon nanosheets in the composites. Therefore, as lithium ion battery anode, the composites exhibited an excellent lithium ion storage capacity, high rate capability, and decent discharge/charge cycling stability. It was demonstrated that the reversible specific capacity can reach 1132 mA h/g at the charge/discharge current density of 0.1 A/g, and it can maintain at 980 mA h/g after 400 cycles. Even at a high current density of 10 A/g, the reversible capacity was still retained above 350 mA h/g, which is much higher than that of other carbon and Fe_3O_4 composites reported so far. These results render the as-prepared composite as one of ideal anode material for high performance lithium ion battery.

Introduction

Owing to their unique morphology and admirable properties, the free-standing two dimensional (2D) materials have been utilized in electronic devices, catalysts, sensors, energy conversion and storage devices, etc.[1-4] In addition, their ultra-large specific surface area and in some cases the abundant surface functional groups render them the optimal template for further fabrication of more complicated nanoarchitectures.[5, 6] In last a few years, the rises of graphene and its derivatives have further prompted research advances in the area.[1-3, 7-9] Up to now, various free-standing 2D materials have been prepared through either top-down or bottom-up approach. When the top-down approach was utilized, the raw materials with intrinsic layered structure are indispensable.[9, 10] For instance, the graphene and its derivatives can be prepared through exfoliation of the graphite as raw materials. Actually, other inorganic 2D materials such as hexagonal boron nitride, vanadium oxide, metal carbides, $Ti_3C_2(OH)_2$, and metal chalcogenides have also been obtained through exfoliation of

the corresponding bulk materials assuming layered structure.[1, 7, 9, 11-18] Alternatively, some free-standing 2D materials were prepared through the bottom-up procedure utilizing the atoms and/or molecules as building blocks. For example, the graphene sheets can also be synthesized with aromatic molecules as precursors,[19] and the thiophene nanosheets were obtained through the self-assembly of the thiophene molecules in certain organic solvents,[3, 8] and so on. Meanwhile the mesoporous free-standing 2D carbon nanomaterials with a few nanometer thicknesses, differing from the pristine graphene, were also fabricated through the bottom-up method, and used in the electrodes of lithium ion battery and supercapacitor.[2, 20] However, it is still challenging to prepare the free-standing 2D materials in bulk scale without template.

Meanwhile, the applications of the free-standing 2D materials have been explored immensely during last decades as well. For instance, the microporous carbon nanoplates containing numerous heteroatoms generated from silk fibroin have been utilized as an electrode in supercapacitors and exhibited impressive electrochemical performance.[2] Similarly,

the mesoporous carbon nanosheets prepared through a low-concentration monomicelle close-packing approach were applied as an anode for lithium ion battaries (LIBs), which displayed an excellent reversible lithium ion capacity.[20] The ferrite/carbon composites assuming 2D morphologies were also employed as LIBs anodes and showed enhanced durability and rate capability.[21] Those pioneering works imply that the 2D materials, especially the carbon based ones, should be greatly promising for novel energy storage devices.

In this work, we developed a scalable hydrothermal approach to prepare the boron-doped free-standing carbon nanosheets using glucose as carbon precursor, and sodium borohydride ($NaBH_4$) as mineralization and structure-directing agent. Moreover, using the as-prepared carbon nanosheets as substrates, dense Fe_3O_4 nanoneedle arrays were fabricated *in situ* on them. Thus, the novel composites of boron-doped carbon nanosheets/Fe_3O_4 nanoneedles were obtained, which assume the free-standing sheet motif as well. Significantly, both the as-prepared bare boron-doped carbon nanosheets and the composites have noteworthy lithium ion storage performances. Expressively, at a high charge/discharge current density of 10 A/g, the reversible specific capacities of the bare carbon nanosheets and the composites can be maintained at 125 and 350 mA h/g, respectively, with exceptional cycling stability. These capabilities should be satisfied for the power lithium ion battery application. The formation mechanism of the novel composite and the origin for their exceptional lithium ion storage performance were also elaborated.

Experimental

Preparation of carbon nanosheets

Boron-doped carbon nanosheets were synthesized through a hydrothermal procedure using glucose as carbon precursor, and $NaBH_4$ as mineralization agent. In a typical experiment, 4 g of glucose and 0.3 g of $NaBH_4$ were dissolved in 40 mL deionized (DI) water. The solution was then transferred into a Teflon-lined autoclave, and heated at 180 °C for 12 h. After being cooled naturally down to room temperature, the solid product (the carbon nanosheets) was separated by centrifugation and washed thoroughly with DI water for three times.

Fabrication of composite of boron-doped carbon nanosheets/Fe_3O_4 nanoneedles

The composite was synthesized by growing Fe_3O_4 directly onto the boron-doped carbon nanosheets in aqueous solution followed by a thermal annealing. First, iron (II) sulfate heptahydrate ($FeSO_4 \cdot 7H_2O$), 180 mg, and iron (III) sulfate hydrate ($Fe_2(SO_4)_3 \cdot xH_2O$), 160 mg, were dissolved into 40 mL of DI water to get a mixed solution containing Fe^{3+} and Fe^{2+} ions. Then, the aqueous solution of the boron-doped carbon sheets (40 mL, 1 mg/mL) was added into the iron ions solution. The mixture was stirred for 10 h at room temperature. The resulting solid product was separated from the reaction mixture by centrifugation and washed three times with DI water. Finally, the composites were annealed in a nitrogen atmosphere at 350 °C for 2 h.

Characterization

SEM images were acquired on an Ultra 55 field emission scanning electron microscope (SEM, Zeiss, Germany). TEM images were obtained using a JEM-2010 transmission electron microscope (JEOL Ltd., Japan). The TEM samples were prepared by putting a droplet of water suspension of the composite on a copper grid, followed by removal of the solvent through tilting the grid on a piece of filter paper. The FT-IR spectra were recorded on an EQUINOX 55 FT-IR spectrometer (Bruker, Germany). The specimens for FT-IR measurement were prepared by grinding the dried powder with KBr together and then compressed into thin pellets. Atomic force microscopic (AFM) images were taken on a MultiMode Nanoscope V scanning probe microscopy system (Veeco, USA). Nitrogen adsorption/desorption isotherms were measured at 77 K on an automated adsorption apparatus (Micromeritics, USA). The surface area was determined using the Brunauer–Emmett–Teller (BET) method. X-ray powder diffraction (XRD) patterns were obtained on a D/max-2600 PC diffractometer (Rigaku, Japan) using Cu/Kα radiation (λ = 1.55406Å). Raman measurements were performed on an Ar ion laser Micro-Raman spectroscope (Jobin Yvon LabRam HR 800 UV, France) with an excitation laser beam wavelength of 514.5 nm.

Electrochemical measurements

Electrochemical experiments were carried out on 2025 type coin cells. In the coin cells, the working electrodes were prepared using the mixture of the as-obtained composites of boron-doped carbon nanosheets /Fe_3O_4 nanoneedles or the bare boron-doped carbon nanosheets (for comparison) with carbon black (Super-P), and poly(vinyldifluoride) (PVDF) with a weight ratio of 8:1:1, which were coated on copper foil. The lithium plate was used as the counter electrode. The electrolyte was 1 M $LiPF_6$ in ethylene carbonate (EC)/dimethyl carbonate (DMC) (1:1, in volume). The cells were assembled in an argon-filled glove box. The electrochemical performance was tested at various current densities in a voltage range of 0.01-3.00 V. The cyclic voltammograms (CV) were obtained over the voltage range from 0.01 to 3.00 V at a scanning rate of 0.1 mV s^{-1} using an electrochemical working station (CHI 660C) (Shanghai, China).
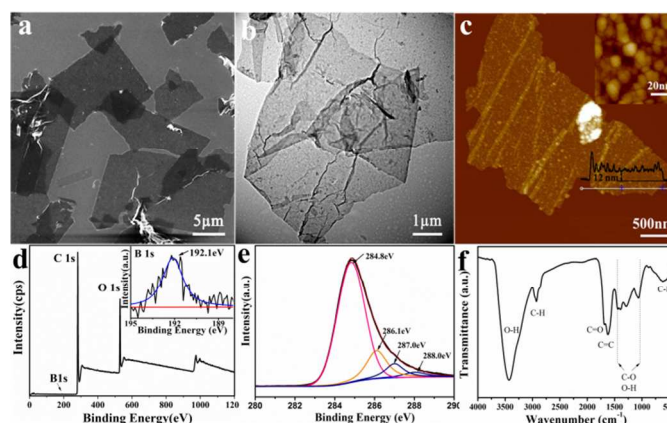
Results and discussion

Fig. 1 a) SEM, b) TEM, and c) AFM images of boron-doped carbon nanosheets. The up-right inset in (c) shows the high resolution AFM image of the boron-doped carbon nanosheests revealing that the nanosheets were composed of nanospheres. The down-right inset in (c) shows the height profile of the nanosheets. d) and e) depict the survey and high resolution XPS spectra of C 1s of the boron-doped carbon nanosheets,

respectively. Inset in d) shows the XPS spectrum of B 1s. f) FT-IR spectrum of the boron-doped carbon nanosheets.

The morphology of the solid products obtained through the hydrothermal reaction of the glucose via $NaBH_4$ as a mineralization agent was first characterized using SEM. It reveals clearly that the solid product assume ultrathin sheet-like structure (Fig. 1a). The lateral dimensions of the individual sheets can reach up to several tens of micrometers. The sheet structural motif was further confirmed with TEM and AFM imaging. As shown in Fig. 1b, the TEM images show that the ultrathin sheets are uniform in thickness. The cross-sectional profile analyses of the AFM image (Fig. 1c) illustrated that the thickness of the as-obtained sheets was about 12 nm. More interestingly, the high-magnification AFM image (Fig. 1c, inset) showed that the nanosheet was actually composed of a large number of nanospheres connected each other. Moreover, some of the nanosheets appeared to be wrinkled and folded, demonstrating their elastic nature. To confirm the detailed chemical composition, the as-obtained nanosheets were subjected to XPS analysis. As shown in Fig. 1d, besides the dominant C and O peaks, the survey spectra showed also a weak peak of B (trace amounts). The atomic concentrations of C, O and B in the nanosheets are 85.43, 14.35, and 0.22%, respectively, estimating from the intensities of the corresponding XPS peaks. This result illustrates that the nanosheets contain a large amount of the oxygen, which might be inherited from the glucose. Fig. 1e shows the C 1s XPS spectrum of the nanosheets. There actually are four peaks centered at 284.8, 286.1, 287.2 and 288.0 eV, which can be assigned to C=C/C-C (carbon backbone), C-O (epoxy and/or alkoxy), C=O (carbonyl), and COOR (carboxylic and/or lactones), respectively.[22,23] These data confirmed further the carbon nanosheets have varied oxygen-containing groups which is agree well with the results of the FT-IR (Fig. 1f) and Raman measurements (ESI, Fig. S1†). In fact, the enrichment of oxygen-containing groups in as-obtained nanosheets is similar to other carbonaceous materials generated from carbohydrates through a hydrothermal procedure.[22,24] Nitrogen-sorption measurements of the boron-doped carbon nanosheets revealed a type-IV isotherm with a type-H3 hysteresis (Fig. 2a), reflecting the porous structure. The Brunauer-Emmett-Teller (BET) specific surface area is about 298 $m^2 g^{-1}$. The major pore size is around 4.2 nm derived from the desorption branch (Fig. 2b).
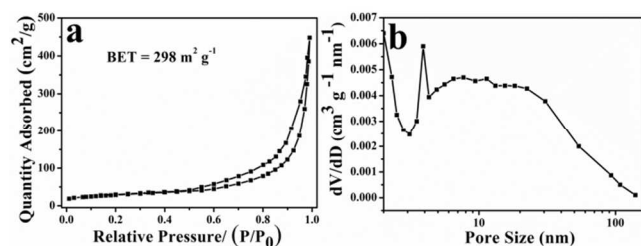

Fig. 2 N_2 adsorption-desorption isotherms and BJH-adsorption pore size distributions of the carbon nanosheets.

In general, through hydrothermal carbonization of glucose and other carbon hydrates, individual carbon nanospheres or even microspheres can be obtained. For the formation mechanism of the individual carbon nano/microspheres, there are several assumptions have been proposed.[22,24-29] Usually, it was believed that the whole procedure for carbon nano/microsphere formation should involve the dehydration, polymerization and aromatization. Differently, as illustrated

above, in this work the as-produced carbon nanospheres interconnected closely forming a sheet structure. The reason
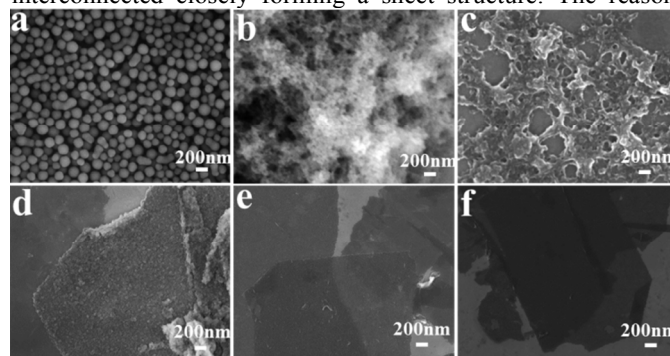

Fig. 3 SEM images of the carbonization products of glucose through hydrothermal reactions with different $NaBH_4$ concentrations of (a) 0 mg/mL, (b) 2.5 mg/mL, (c) 5 mg/mL, (d) 7 mg/mL, (e) 7.5 mg/mL, (f) 9 mg/mL, but with the same concentration of glucose.

might be that the $NaBH_4$ was utilized as a mineralization agent. To elaborate the role of $NaBH_4$ in the formation of the carbon nanosheets, a series of control experiments were conducted by varying the concentration of $NaBH_4$ in the reaction solution, but keeping the concentration of glucose constantly. As depicted in Fig. 3a, without $NaBH_4$, the products showed uniform nanospherical morphology. When the concentration of $NaBH_4$ was 2.5 mg/mL, some of the as-produced carbon nanospheres started to link each other, Fig. 3b. If the concentration of $NaBH_4$ was increased to 5 mg/mL, the carbon nanospheres connected more closely showing partial sheet-like feature, Fig. 3c. Once the concentration is over 7 mg/mL, the nanospheres connected tightly each other forming carbon sheets, Fig. 3b-f. These results demonstrated unambiguously the $NaBH_4$ plays a critical role in the formation of carbon nanosheets through the hydrothermal carbonization of glucose. It is well known that the $NaBH_4$ can be hydrated into $BO(OH)_2$, which assumes triangle plane symmetry. The hydroxyl groups of the $BO(OH)_2$ may condense with hydroxyl groups from carbon nanospheres under the hydrothermal condition. As a result, the carbon nanospheres were interlinked by boron-oxygen-carbon bonds forming finally the boron-doped carbon sheets. This result leads us to believe that the $NaBH_4$ plays dual roles, a mineralization and structure directing reagent in glucose mineralization.[29, 30] The proposed mechanism for the formation of boron-doped carbon nanosheets was schematically presented in Scheme 1.
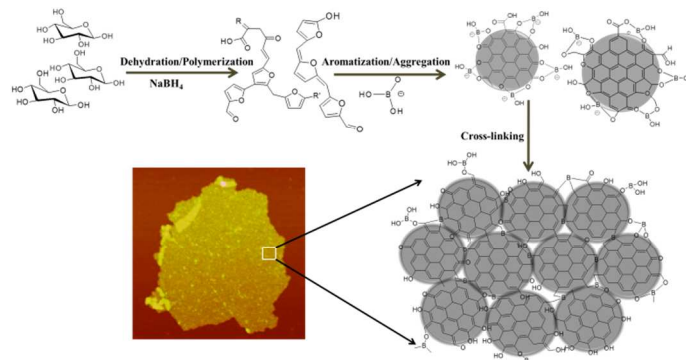
Scheme 1 Schematic illustration of the formation mechanism for the boron-doped carbon nanosheets.

As illustrated above by FT-IR and XPS data, the as-prepared boron-doped carbon nanosheets have abundant surface oxygen containing groups. These groups in principle can serve as the initial or anchoring sites for generation or deposition of other nanomaterials on them. From a chemistry point of view, the as-prepared carbon nanosheets should be the optimal template for growing directly metal oxide nanoparticles on them, because they are rich with oxygen containing groups, which is similar to the graphene oxide sheets. In our previous work, the Fe_3O_4 nanoparticles with different sizes and morphologies have been controllably fabricated on the graphene oxide sheets.[31] Considering also that the Fe_3O_4 showed extraordinary physical/chemical properties, and has been utilized in biological systems, catalysts, energy storage devices, etc,[32-34] we first tried to generate the precursor of Fe_3O_4, most probably iron oxyhydroxide (FeOOH), on the boron-doped carbon nanosheets by simply mixing the aqueous solutions of $FeSO_4$ and $Fe_2(SO_4)_3$ with the suspension of the boron-doped carbon sheets at room temperature. As depicted in ESI Fig. S2† a and b, after 10 h of reaction, high density nanoneedle array grew onto the boron-doped carbon sheets uniformly. The XRD pattern (ESI, Fig. S2c†) revealed that iron oxyhydroxide (FeOOH) was obtained in this process. Owing to the poor cycling stability of FeOOH (ESI, Fig. S3a†) and the bare boron-doped carbon sheets containing certain oxygen groups for the irreversible lithium ion storage of the electrode materials (ESI, Fig. S3b†),[35,36] The as-obtained nanocomposites were further subjected to annealing at 350 °C for 2 h in nitrogen atmosphere to convert FeOOH to Fe_3O_4 and, at the same, reduce somehow the oxygen groups from boron-doped carbon nanosheets.[35, 37, 38] The SEM images, Fig. 4a, b, showed that the high density nanoneedle array motif was preserved well after the annealing, the average dimensions of the individual nanoneedles are about 8 nm in diameter and ~150 nm in length and were arranged with their long axes almost perpendicular to the carbon nanosheets. To elaborate the composition and also the structure of the as-generated nanoneedles, the X-ray powder diffraction (XRD) patterns of the nanocomposites after the annealing were obtained. As shown in ESI Fig. S4†, the diffraction peaks can be indexed to the crystalline Fe_3O_4 (JCPDS no. 19-0629). To ratify the formation of crystalline Fe_3O_4 nanoneedles, but not the Fe_2O_3, thermogravimetry analysis (TGA) was conducted. It is well known that the Fe_3O_4 can be oxidized to Fe_2O_3 with a weight gain in air in the temperature range of 150-400 °C.[39, 40] As expected, the TGA data, (ESI, Fig. S5†) revealed that the weight gain, about 2.5 %, did happen at 150-270 °C. In addition, as seen from the HRTEM image (Fig. S6†), the interplanar of 0.25 nm fits well with the d-spacing of (311) plane of Fe_3O_4.[31,34] These data further confirmed the formation of the ultrahigh density arrays of Fe_3O_4 nanoneedles on the boron-doped carbon nanosheets. For comparison, the pure boron-doped carbon nanosheets were also annealed under the same conditions, the SEM images, Fig. 4c, d, showed that the morphology of the nanosheets were preserved well after the annealing. The FT-IR spectrum and XRD patterns of the sample demonstrated that the most oxygen-containing groups have been removed and the degree of graphitization was enhanced after annealing (ESI, Fig. S7†). The main text of the article should go here with headings as appropriate.

Considering the unique hierarchical morphology and composition, the carbon nanosheets can serve as efficient charge (ions and electron) transportation media, and the nanostructured Fe_3O_4 has been shown potential in anode of lithium ion battery owing to its high theoretical capacity,[41-45]

it's reasonable to expect the as-prepared nanocomposites will exhibit exceptional electrochemical properties as anode for LIBs. In addition, in the as-prepared nanocomposites, the Fe_3O_4 nanoneedles can work as structural spacers to suppress the aggregation of the carbon nanosheets during the processing and long term applications. Moreover, the abundant voids in Fe_3O_4 nanoneedle arrays in the composites may also increase the contacting efficiency of the electrode with the electrolyte and fast the ion transport. Thereby, the as-prepared composites in principle will meet the requirements of anode materials for high performance LIBs.
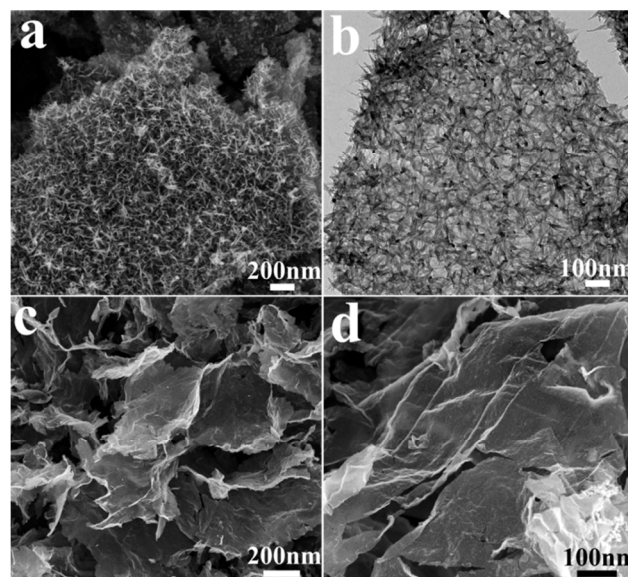

Fig. 4 (a) SEM and (b) TEM images of the composite of carbonized boron-doped carbon nanosheets and Fe_3O_4 nanoneedles; (c, d) SEM images of the pure carbonized boron-doped carbon nanosheets.

To evaluate the electrochemical performances of the composites of boron-doped carbon sheets and Fe_3O_4 nanoneedles as LIB anodes, half coin cells were assembled using the lithium metal plate and as-prepared composites coated on the copper foil as electrodes. Fig. 5a presents the cyclic voltammograms (CVs) of the as-assembled coin cells. Three peaks at 1.5, 0.55, and 0.02 V were detected during the first discharging cycles, and another one peak at 1.8 V was also observed during the first charging cycle. The peak at 0.55 V can be assigned to the reduction processes of Fe_3O_4 (Fe_3O_4 + $8Li^+$ + $8e^-$ = $3Fe^0$ + $4Li_2O$), electrolyte decomposition and inevitable formation of solid electrolyte interface (SEI) layer. The peak at 1.5 V, which is absent in the following cycle, might be attributed to the formation of $Li_xFe_3O_4$. The peak at 0.02 V mainly corresponds to the lithium ions insertion in the boron doped carbon sheets. The broad peak at 1.8 V is attributed to the oxidation of Fe to Fe_3O_4, which is in good agreement with the previous reports.[34, 37, 46] Starting from the second cycle, all of the cathode and anode peaks positively shifted due might to the polarization of the electrode during the charge/discharge cycles. Notably, the CV curves almost overlapped after the first cycle, indicating good electrochemical reversibility. Fig. 5b shows the representative discharge/charge voltage profiles of the coin cell at a current density of 0.1 A/g within a voltage window of 0.01-3 V. The electrode of the composite of boron-doped carbon sheets and Fe_3O_4 nanoneedles has the first discharge and charge capacities of 1672.8 and 1132.1 mAh/g,

respectively. The estimated coulombic efficiency (CE) of the first cycle is ~ 68%. The irreversible capacity loss in the first cycle is due to the irreversible processes such as electrolyte decomposition and inevitable formation of SEI film. These data are in agreement with the aforementioned CV results. The as-measured discharge and charge capacities for the second cycle are 1187.9 and 1085.1 mA h/g, respectively. The CE for the second cycle discharge and charge was increased rapidly to 91.3%. It is worth pointing out that, after 10 cycles, the discharge capacity of the coin cells still remains as high as 1061 mA h/g, and the CE reaches nearly 98%. When the charge/discharge current densities were increased to 0.2, 0.4, 0.6, 0.8, 1, 2, 5, and 10 A/g, the as-measured specific capacity of the coin cell were 1000, 970, 830, 780, 750, 670, 510 and 350 mA h/g, respectively, revealing the good rate capability. Remarkably, it was found that even after charge/discharge over 300 cycles at the current density of 0.1 A/g, the specific capacity of the coin cell was remained as high as 980 mA h/g (Fig. 5c) demonstrating the good cycling stability. Additionally, it could be noted that the capacity of the composite is higher than the theoretical capacity of Fe_3O_4, the reason might be ascribed to the ultra-large active surface area and the formation of a pseudo-capacitive gel-like film which actually were observed in other composites containing the nanoscaled metal oxide. [34,38,39,47] Meanwhile, the electrochemical properties of bare boron-doped carbon nanosheets, that were annealed at 350 °C for 2 h in nitrogen atmosphere, were studied on the similar coin cells as well. As shown in Fig. 5c, at a discharge/charge current density of 0.1 A/g, the reversible specific capacity can reach 720.9 mAh/g. The specific capacities were maintained at 330, 230, 125 and 105 mAh/g, when the discharge/charge current densities were increased to 0.5, 2, 10 and 20 A/g, respectively. Notably, after 80 cycles at varied current densities, the capacity is retained at 460 mAh/g when the current density is reset to 0.1 A/g which is much higher than that of other 2D carbon-based materials reported so far.[20,48-50] Moreover, the specific capacity increased continuously with increasing cycling numbers. The reason might be that the number of active sites for Li ion storage was gradually activated during cycling, which was observed within other nanocomposite materials.[51,52] The overall
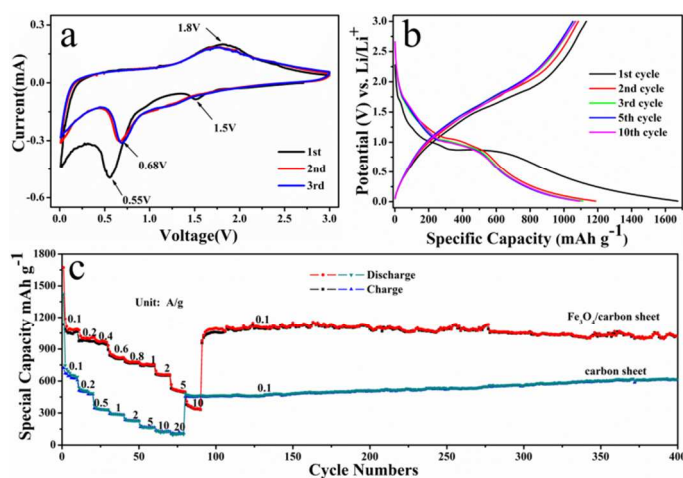

performance of bare boron-doped carbon nanosheets and the composite of boron-doped carbon nanosheets/Fe_3O_4 nanoneedles at different current densities.

electrochemical performances of the composites seem more pronounced than those of the bare boron-doped carbon nanosheets or iron oxides as a working electrode in lithium ion battery.[16,35,53,54] Additionally, in contrast to the conventional anode materials, the hierarchical structural composites exhibit not only a substantially larger lithium ion storage capacity at high current densities, but also excellent cycling stability.

The manifest electrochemical performances of the as-prepared composites should be originated from the synergy effect of boron-doped carbon nanosheets and the chemically bonded Fe_3O_4 nanoneedles on them. Because the boron-doped carbon nanosheets are composed of the carbon nanoparticles interlinked each other, they provided not only large specific surface area, but also abundant pores. These structural characters are desired for lithium ions intercalation and adsorption, which lead finally to large specific capacity. Moreover, the presence of boron within the carbon sheets can also enhance the lithium ion storage capacity and electrical conductivity.[55, 56] Importantly, the boron-doped carbon sheets within electrode can also serve as electron collector and transporter owing to its lower resistance than that of the composites which was illustrated by the electrochemical impedance spectroscopic data (ESI, Fig. S8†). It, therefore, could also reduce Ohmic polarization and enhance the rate capability of the electrodes. The unique nanoneedle morphology, the perpendicular orientation, and the high residual stability of the Fe_3O_4 nanoneedles can suppress largely the aggregation of the boron-doped carbon nanosheets during the charge/discharge that afford the coin cells with high discharge/charge cycling stability. Actually, the SEM image of the anode materials acquired after 400 discharging/charging cycles at a current of 100 mA/g demonstrated that the morphology of the composite was preserved very well (ESI, Fig. S9†). Additionally, the hierarchical structure of the composite not only allows the easy-diffusion of the electrolyte into the inner region of the electrode, but also can accommodate a more sufficient space to sustain the volume variation during the lithium ions insertion and extraction, which may enhance the safety of the battery. These results show that the as-prepared composite of boron-doped carbon nanosheets/Fe_3O_4 nanoneedles should be one of potential candidates for high performance anode materials in lithium-ion battery.

Conclusions

A novel hydrothermal approach to the preparation of boron-doped carbon nanosheets has been developed using glucose and sodium borohydride as precursors. It was demonstrated that the sodium borohydride plays a dual roles in dehydration of glucose, and cross-linking the carbon nanosphenes to form the boron-doped carbon nanosheets. Using the as-fabricated boron-doped carbon nanosheets as substrates, the high density Fe_3O_4 nanoneedle arrays were generated on them. The electrochemical properties of the composites of boron-doped carbon nanosheets with Fe_3O_4 nanoneedles as a lithium ion battery anode were investigated systematically. It was illustrated that the composites exhibited excellent lithium ion storage capacity, high rate capability, and decent discharge/charge cycling stability. The reversible specific capacity of the anode made of the composite can reach 1132.1 mAh/g at the charge/discharge current density of 0.1 A/g, and it

Fig. 5 (a) The first three consecutive CVs of the composite of boron-doped carbon sheets and Fe_3O_4 nanoneedles acquired at a scan rate of 0.1 mV/s. b) The discharge-charge voltage profiles of the 1st, 2nd, 3rd, 5th, and 10th cycle revealing the manifest the coulombic efficiency. c) The discharge/charge cycling

can maintain at 980 mAh/g after 400 charge/discharge cycles. Even at high current density of 10 A/g, the reversible capacity still retained above 350 mAh/g. We believed that the excellent electrochemical performances of the composites should be from the synergy effects of boron-doped carbon nanosheets and the Fe_3O_4 nanoneedles, especially the needle-like morphology and the perpendicular orientation of the Fe_3O_4 nanoneedles within the composite. We envisage that the as-prepared composites should be useful in high performance lithium ion batteries as anode.

Acknowledgements

Notes and references

[a] Key Laboratory for Thin Film and Microfabrication of the Ministry of Education, Research Institute of Micro/Nano Science and Technology, Shanghai Jiao Tong University, Shanghai 200240, P. R. China Tel/Fax: 0086-21-34206915, E-mail: swguo@sjtu.edu.cn, haixiawu@sjtu.edu.cn
[b] School of Materials Science and Engineering, Shaanxi University of Science and Technology, Xi'an, Shaanxi 710021, P. R. China.
† Electronic Supplementary Information (ESI) available: [details of any supplementary information available should be included here]. See DOI: 10.1039/b000000x/

1 X. Huang, Z. Zeng, H. Zhang, *Chem. Soc. Rev.*, 2013, **42**, 1934.
2 Y. S. Yun, S. Y. Cho, J. Shim, B. H. Kim, S. J. Chang, S. J. Baek, Y. S. Huh, Y. Tak, Y. W. Park, S. Park, H. J. Jin, *Adv. Mater.*, 2013, **25**, 1993.
3 Y. Zheng, H. Zhou, D. Liu, G. Floudas, M. Wagner, K. Koynov, M. Mezger, H.-J. Butt, T. Ikeda, *Angew. Chem. Int. Ed.*, 2013, **52**, 4845.
4 Z. Li, H. Zhu, K. Wang, J. Wei, X. Gui, X. Li, C. Li, L. Fan, P. Sun, D. Wu, *Carbon*, 2011, **49**, 237.
5 F. Li, L. Li, X. Liao, L. Tong, Z. Chen, Y. Wang, *Eur. J. Inorg. Chem.*, 2010, **2010**, 4367.
6 M. Baikousi, K. Dimos, A. B. Bourlinos, R. Zbořil, I. Papadas, Y. Deligiannakis, M. A. Karakassides, *Appl. Surf. Sci.*, 2012, **258**, 3703.
7 Y. Du, Z. Yin, J. Zhu, X. Huang, X.-J. Wu, Z. Zeng, Q. Yan, H. Zhang, *Nature Commun.*, 2012, **3,** 1177.
8 Z. Yu, H. Yan, K. Lu, Y. Zhang, Z. Wei, *RSC Adv.*, 2012, **2**, 338.
9 Z. Zeng, T. Sun, J. Zhu, X. Huang, Z. Yin, G. Lu, Z. Fan, Q. Yan, H. H. Hng, H. Zhang, *Angew. Chem. Int. Ed.*, 2012, **51**, 9052.
10 Z. Zeng, Z. Yin, X. Huang, H. Li, Q. He, G. Lu, F. Boey, H. Zhang, *Angew. Chem. Int. Ed.*, 2011, **50**, 11093.
11 X. Wang, C. Zhi, Q. Weng, Y. Bando, D. Golberg, *J. Phys.: Conference Series*, 2013, **471**, 012003.
12 X. Wang, A. Pakdel, J. Zhang, Q. Weng, T. Zhai, C. Zhi, D. Golberg, Y. Bando, *Nanoscale Res. Lett.*, 2012, **6**, 662.
13 M. Wei, Z. M. Qi, M. Ichihara, M. Hirabayashi, I. Honma, H. Zhou, *J. Crys. Growth*, 2006, **296**, 1.
14 T. Yao, L. Liu, C. Xiao, X. Zhang, Q. Liu, S. Wei, Y. Xie, *Angew. Chem, Int. Ed.*, 2013, **52**, 7554.
15 S. Z. Butler, S. M. Hollen, L. U. Cao, Y. Cui, J. A. Gupta, H. R. Gutierrez, T. F. Heinz, S. S. Hong, J. X. Huang, A. F. Ismach, E. Johnston-Halperin, M. Kuno, V. V. OPlashnitsa, R. D. Robinson, R. S. Ruoff, S. Salahuddin, J. Shan, L. Shi, M. G. Spencer, M. Terrones, W. Windl, J. E. Goldberger, *ACS Nano*, 2013, **7**, 2898.
16 M. Chhowalla, H. S. Shin, G. Eda, L. J. Li, K. P. Loh, H. Zhang, *Nature Chem.*, 2013, **5**, 263.
17 C. Zhu, Z. Zeng, H. Li, F. Li, C. Fan, H. Zhang, *J. Am. Chem. Soc.*, 2013, **135**, 5998.
18 H. Li, G. Lu, Y. Wang, Z. Yin, C. Cong, Q. He, L. Wang, F. Ding, T. Yu, H. Zhang, *Small*, 2013, **9**, 1974.
19 J. Wu, W. Pisula, K. Mullen, *Chem. Rev.*, 2007, **107**, 718.
20 Y. Fang, Y. Lv, R. Che, H. Wu, X. Zhang, D. Gu, G. Zheng, D. Zhao, *J. Am. Chem. Soc.*, 2013, **135**, 1524.
21 B. Jang, M. Park, O. B. Chae, S. Park, Y. Kim, S. M. Oh, Y. Piao, T. Hyeon, *J. Am. Chem. Soc.*, 2012, **134**, 15010.
22 M. Sevilla, A. B. Fuertes, *Chem. Eur. J.*, 2009, **15**, 4195.
23 M. Li, W. Li, S. Liu, *Carbohydr. Res.*, 2011, **346**, 999.
24 X. Sun, Y. Li, *Angew. Chem. Int. Ed.*, 2004, **43**, 597.
25 K. Pan, H. Ming, Y. Liu, Z. Kang, *New J. Chem.*, 2012, **36**, 113.
26 G. H. Jiang, X. Q. Xu, G. Xu, *Mater. Sci. Forum*, 2011, **685**, 123.
27 Y. Shin, L. Q. Wang, I. T. Bae, B. W. Arey, G. J. Exarhos, *J. Phys. Chem. C.*, 2008, **112**, 14236.
28 J. Ryu, Y. W. Suh, D. J. Suh, D. J. Ahn, *Carbon*, 2010, **48**, 1990.
29 T. P. Fellinger, R. J. White, M. M. Titirici, M. Antonietti, *Adv. Funct. Mater.*, 2012, **22**, 3254.
30 R. Nishiyabu, Y. Kubo, T. D. James, J. S. Fossey, *Chem. Commun.*, 2011, **47**, 1124.
31 H. Wu, G. Gao, X. Zhou, Y. Zhang, S. Guo, *CrystEngComm*, 2012, **14**, 499.
32 X. Shi, S. H. Wang, S. D. Swanson, S. Ge, Z. Cao, M. E. Van Antwerp, K. J. Landmark, J. R. Baker, *Adv. Mater.*, 2008, **20**, 1671.
33 R. Liu, Y. Guo, G. Odusote, F. Qu, R. D. Priestley, *ACS Appl. Mater. Interfaces*, 2013, **5**, 9167.
34 C. Wang, Q. Zhang, Q. H. Wu, T. W. Ng, T. Wong, J. Ren, Z. Shi, C. S. Lee, S. T. Lee, W. Zhang, *RSC Adv.*, 2012, **2**, 10680.
35 Z. Xiao, Y. Xia, Z. Ren, Z. Liu, G. Xu, C. Chao, X. Li, G. Shen, G. Han, *J. Mater. Chem.*, 2012, **22**, 20566.
36 C. Zhang, J. Zhu, X. Rui, J. Chen, D. Sim, W. Shi, H. H. Hng, T. M. Lim, Q. Yan, *CrystEngComm*, 2012, **14**, 147.
37 J. E. Lee, S. H. Yu, D. J. Lee, D. C. Lee, S. I. Han, Y. E. Sung, T. Hyeon, *Energy Environ. Sci.*, 2012, **5**, 9528.
38 C. Ban, Z. Wu, D. T. Gillaspie, L. Chen, Y. Yan, J. L. Blackburn, A. C. Dillon, *Adv. Mater.*, 2010, **22**, 145.
39 Y. Dong, R. Ma, M. Hu, H. Cheng, Q. Yang, Y. Y. Li, J. A. Zapien, *Phys. Chem. Chem. Phys.* 2013, **15**, 7174.
40 J. Liu, Y. Zhou, F. Liu, C. Liu, J. Wang, Y. Pan, D. Xue, *RSC Adv.*, 2012, **2**, 2262.
41 P. Poizot, S. Laruelle, S. Grugeon, L. Dupont, J. M. Tarascon, *Nature* 2000, **407**, 496.
42 B. Wang, H. B. Wu, L. Zhang, X. W. D. Lou, *Angew. Chem. Inter. Ed.*, 2013, **52**, 4165.
43 L. Zhang, H. B. Wu, S. Madhavi, H. H. Hng, X. W. Lou, *J. Am. Chem. Soc.*, 2012, **134**, 17388.
44 J. Chen, L. Xu, W. Li, L. X, Gou, *Adv. Mater.*, 2005, **17**, 582.
45 Y. Liu, W. Zhang, Y. Zhu, Y. Luo, Y. Xu, A. Brown, J. N. Culver, C.

A. Lundgren, K. Xu, Y. Wang, C. Wang, *Nano Lett.*, 2013, **13**, 293.

46   Z. Xiao, Y. Xia, Z. Ren, Z. Liu, G. Xu, C. Chao, X. Li, G. Shen, G. Han, *J. Mater. Chem.*, 2012, **22**, 20566.

47   S. L. Chou, J. Z. Wang, D. Wexler, K. Konstantinov, C. Zhong, H. K. Liu, S. X. Dou, *J. Mater. Chem.*, 2010, **20**, 2092.

48   L. Chen, Z. Wang, C. He, N. Zhao, C. Shi, E. Liu, J. Li, *ACS Appl. Mater. Interfaces*, 2013, **5**, 9537.

49   P. Lian, X. Zhu, S. Liang, Z. Li, W. Yang, H. Wang, *Electrochim. Acta*, 2010, **55**, 3909.

50   D. Pan, S. Wang, B. Zhao, M. Wu, H. Zhang, Y. Wang, Z. Jiao, *Chem. Mater.*, 2009, **21**, 3136.

51   Y. S. Yun, H. J. Jin, *Mater. Lett.*, 2013, **108**, 311.

52   G. P. Kim, S. Park, I. Nam, J. Park, J. Yi, *J. Mater. Chem. A*, 2013, **1**, 3872.

53   J. Chen, L. Xu, W. Li, X. Gou, *Adv. Mater.*, 2005, **17**, 582.

54   J. Zhu, Z. Yin, D. Yang, T. Sun, H. Yu, H. E. Hoster, H. H. Hng, H. Zhang, Q. Yan, *Energy Environ. Sci.*, 2013, **6**, 987.

55   L. Qie, W. M. Chen, Z. H. Wang, Q. G. Shao, X. Li, L. X. Yuan, X. L. Hu, W. X. Zhang, Y. H. Huang, *Adv. Mater.*, 2012, **24**, 2047.

56   Z. S. Wu, W. C. Ren, L. Xu, F. Li, H. M. Cheng, *ACS Nano*, 2011, **5**, 5463.